Front. Phys. 13(4), 130311 (2018)
https://doi.org/10.1007/s11467-018-0778-y

RESEARCH ARTICLE

Self-trapping under two-dimensional spin-orbit coupling and spatially growing repulsive nonlinearity

Rong-Xuan Zhong[1], Zhao-Pin Chen[2], Chun-Qing Huang[1], Zhi-Huan Luo[3], Hai-Shu Tan[1], Boris A. Malomed[2,4,1], Yong-Yao Li[1,†]

[1] *School of Physics and Optoelectronic Engineering, Foshan University, Foshan 528000, China*
[2] *Department of Physical Electronics, School of Electrical Engineering, Faculty of Engineering, Tel Aviv University, Tel Aviv 69978, Israel*
[3] *College of Electronic Engineering, South China Agricultural University, Guangzhou 510642, China*
[4] *ITMO University, St. Petersburg 197101, Russia*
Corresponding author. E-mail: [†] *yongyaoli@gmail.com*
Received December 7, 2017; accepted March 3, 2018

We develop a method for creating two- and one-dimensional (2D and 1D) self-trapped modes in binary spin-orbit-coupled Bose–Einstein condensates with the contact repulsive interaction, whose local strength grows sufficiently rapidly from the center to the periphery. In particular, an exact semi-vortex (SV) solution is found for the anti-Gaussian radial modulation profile. The exact modes are included in the numerically produced family of SV solitons. Other families, in the form of mixed modes (MMs), as well as excited states of SVs and MMs, are also produced. Although the excited states are unstable in all previously studied models, they are partially stable in the present one. In the 1D version of the system, exact solutions for the counterpart of SVs, namely, semi-dipole solitons, are also found. Families of semi-dipoles, as well as the 1D version of MMs, are produced numerically.

Keywords spin-orbit coupling, semi-vortex, mixed mode, excited states

PACS numbers 03.75.Lm, 05.45.Yv

1 Introduction

Prediction and experimental creation of stable two- and three-dimensional (2D and 3D) solitons has long been a challenging problem in nonlinear physics. A well-known difficulty is that fundamental multidimensional solitary modes in 2D and 3D media with the ubiquitous cubic self-focusing nonlinearity are made unstable by critical and supercritical collapse, respectively [1, 2] in the 2D and 3D geometry. Solitons with embedded vorticity (also known as vortex rings and tori) [3] are destabilized by a still stronger azimuthal splitting instability. Development of methods for stabilization of multidimensional fundamental and vortex solitons is of great interest for nonlinear photonics and mean-field dynamics in Bose–Einstein condensates (BECs) [4–11].

A method that makes it possible to produce exceptionally robust multidimensional modes is based on use of repulsive (defocusing) nonlinearity, whose local strength grows from the center to the periphery, in a space of dimension D at any rate faster than R^D, as demonstrated in a number of theoretical works [12–20]. This type of nonlinearity modulation can be induced using various techniques. In optical media, one may use nonlinearity-enhancing dopants with an inhomogeneous density [21]. In BECs, the tunability of the local nonlinearity using the magnetic Feshbach resonance (FR) [22, 23] suggests the possibility of creating spatially modulated nonlinearity profiles using appropriately shaped magnetic fields [24], which was realized in an experiment [25]. Furthermore, nearly arbitrary spatial profiles of the self-repulsive nonlinearity can be imposed by using the optically controlled FR [26, 27] or combined magneto-optical shaping [28]. A nonlocal version of this setting may be realized in terms of the long-range interaction between dipolar moments locally induced by a nonuniform dc electric field [29–33].

The other promising method for stabilization of 2D and 3D solitons relies upon the use of the effective spin-orbit (SO) coupling in binary condensates. The possi-

*arXiv: 1712.01430.

bility of emulating the effects of SO coupling, originally known in the physics of semiconductors, in two-component atomic BECs has been demonstrated experimentally and analyzed in detail theoretically [34–41]. As the SO coupling in BECs is a linear interaction between spatially inhomogeneous states in the two components, its interplay with the intrinsic nonlinearity of the BEC makes it possible to predict diverse nonlinear phenomena [42–65]. In particular, a noteworthy result that opens the way to novel applications of SO coupling in studies of matter waves is the stabilization of 2D solitons in free space in the form of semi-vortices (SVs) (also known as half-vortices [44]), where the vorticity is carried by one component of the spinor complex, and mixed modes (MMs), which combine terms with zero and nonzero vorticities in each component [69–71]. These results break a commonly adopted paradigm stating that bright solitons supported by cubic self-attractive nonlinearities in free space are always unstable owing to the presence of critical collapse in the same system [1, 2]. In other words, stable SVs and MMs act as the ground state, which is missing in the 2D free-space settings with cubic self-attraction, in the absence of SO coupling [69, 70].

In optics, it has been demonstrated that spatiotemporal solitons in a planar dual-core Kerr-nonlinear waveguide can be stabilized by temporal dispersion of the linear coupling between the cores, which provides an optical counterpart of SO coupling [72]. Further, regarding emulation of SO coupling in photonics, attention was recently drawn to effects in exciton-polariton condensates in microcavities [73–76].

It was found that in three dimensions, the interplay of SO coupling with attractive cubic nonlinearity in free space creates metastable 3D solitons of the same types as in two dimensions, viz., SVs and MMs [77]. SO coupling also helps one to build stable solitons under the action of long-range dipole–dipole interactions in binary BECs. As reported in Refs. [78–80], these may be striped modes and anisotropic vortices, as well as stable 2D gap solitons, supported by a combination of SO coupling and Zeeman splitting, when the kinetic energy terms may be neglected in the corresponding 2D system [65, 66]. The peculiarities of collapse in SO-coupled systems were explored in Refs. [67] and [68].

The objective of this work is to study solitons in a setting that has not been explored, namely, SO coupling acting in combination with self-repulsive contact nonlinearity, which induces self-trapping owing to the growth of its local strength from the center to the periphery, similar to the behavior introduced (in the absence of SO coupling) in Refs. [12] and [13]. In particular, we find stable analytical solutions for 2D solitons of the SV type, which, to the best of our knowledge, are the first example of solitons available in an exact form under the action of SO coupling. Stable 2D solitons of the MM type, as well as unstable excited states of SVs and MMs, are found in a numerical form. Exact soliton solutions are also reported for the one-dimensional (1D) version of the spinor system.

The paper is structured as follows. The model is introduced in Section 2, which is followed by a presentation of the analytical and numerical solutions for SV solitons and the results for their stability in Section 3. Solitons of the MM type are addressed using numerical methods in Section 4. Further, excited states of SVs and MMs are considered in Section 5. Exact analytical solutions and families of numerically obtained ones for the 1D version of the system are considered in Section 6. The paper is concluded in Section 7.

2 The model

In the usual mean-field approximation, the evolution of the spinor wave functions of the spinor BEC, $\psi = (\psi_+, \psi_-)$, is governed by the coupled Gross–Pitaevskii equations (GPEs), which include SO coupling of the Rashba type [81, 82]:

$$\begin{aligned} \mathrm{i}\partial_t \psi_\pm = &-\frac{1}{2}\nabla^2\psi_\pm + \exp(r^2)\cdot(|\psi_\pm|^2 + \gamma|\psi_\mp|^2)\psi_\pm \\ &\pm\lambda(\partial_x \mp \mathrm{i}\partial_y)\psi_\mp. \end{aligned} \tag{1}$$

The equations are written in the scaled form; λ is the normalized strength of the SO coupling, and γ is the relative strength of the cross-interaction between the two components with respect to the self-repulsion. Strictly speaking, the magnetic field, which imposes the necessary FR landscape, may have different effects on the two hyperfine atomic states making up the SO-coupled system. In the present model, we neglect the difference to obtain analytical solutions. Additional numerical results suggest that, if it is considered, the difference does not produce noticeable changes in the results.

In physical units, the SO coupling strength is characterized by the ratio of the corresponding length scale, a_{SO}, to the confinement length, $a_\perp$, which makes it possible to reduce the 3D GPEs to the 2D form. In real experiments, this ratio is usually $a_{\mathrm{SO}}/a_\perp \sim 0.1$ [34, 44]. The modulation profile of the repulsive nonlinearity in Eq. (1) is adopted in the anti-Gaussian form, as it makes it possible to find particular exact solutions for the self-trapped states [13]. Qualitatively, this steep profile does not yield results dramatically different from those produced by milder profiles [12, 13].

As usual, stationary states with chemical potential μ are searched for, $\psi_\pm(x,y,t) = \phi_\pm(x,y)\mathrm{e}^{-\mathrm{i}\mu t}$, where $\phi_\pm$ represents complex stationary wave functions. These states are characterized by the total norm, which is proportional to the number of atoms in binary BECs:

$$N = N_+ + N_- = \iint (|\psi_+|^2 + |\psi_-|^2)\mathrm{d}x\mathrm{d}y. \tag{2}$$

Further, the total energy of the soliton is

$$E = E_{\mathrm{K}} + E_{\mathrm{N}} + E_{\mathrm{SO}}, \tag{3}$$

where E_{K} is the kinetic term, and E_{N} and E_{SO} are the energies of the nonlinear and SO interactions, respectively:

$$\begin{aligned} E_{\mathrm{K}} &= \frac{1}{2}\int \mathrm{d}\boldsymbol{r}(|\nabla\psi_+|^2 + |\nabla\psi_-|^2), \\ E_{\mathrm{N}} &= \frac{1}{2}\int \mathrm{d}\boldsymbol{r}\mathrm{e}^{r^2}(|\psi_+|^4 + |\psi_-|^4 + 2\gamma|\psi_+|^2|\psi_-|^2), \\ E_{\mathrm{SO}} &= \lambda\int \mathrm{d}\boldsymbol{r}\left[\psi_+^*\left(\partial_x - \mathrm{i}\partial_y\right)\psi_- - \psi_-^*\left(\partial_x + \mathrm{i}\partial_y\right)\psi_+\right]. \end{aligned} \tag{4}$$

For SV solitons, ψ_+ and ψ_- are defined as the zero-vorticity and vortical components, respectively. In fact, SVs are the simplest axisymmetric fundamental modes existing in the system. It is relevant to define the relative share of the total norm carried by the vortex component:

$$F_- = N_-/N. \tag{5}$$

The stability of the solitons was investigated numerically by computing the eigenvalues for small perturbations, and the results were subsequently verified by direct simulations of Eq. (1). To this end, the perturbed solution was taken as

$$\psi_\pm = (\phi_\pm + u_\pm \mathrm{e}^{-\mathrm{i}\Lambda t} + v_\pm^* \mathrm{e}^{\mathrm{i}\Lambda^* t})\mathrm{e}^{-\mathrm{i}\mu t}, \tag{6}$$

where $*$ represents the complex conjugate. The substitution of this expression into Eq. (1) and linearization yield a system of four equations:

$$\begin{aligned} (\mu+\Lambda)u_+ &= -\frac{1}{2}\nabla^2 u_+ + \lambda(\partial_x - \mathrm{i}\partial_y)u_- \\ &\quad + \mathrm{e}^{r^2}\left(2|\phi_+|^2 + \gamma|\phi_-|^2\right)u_+ \\ &\quad + \mathrm{e}^{r^2}\left(\phi_+^2 v_+ + \gamma\phi_+\phi_- v_- + \gamma\phi_-^*\phi_+ u_-\right), \\ (\mu+\Lambda)u_- &= -\frac{1}{2}\nabla^2 u_- - \lambda(\partial_x + \mathrm{i}\partial_y)u_+ \\ &\quad + \mathrm{e}^{r^2}\left(2|\phi_-|^2 + \gamma|\phi_+|^2\right)u_- \\ &\quad + \mathrm{e}^{r^2}\left(\phi_-^2 v_- + \gamma\phi_-\phi_+ v_+ + \gamma\phi_+^*\phi_- u_+\right), \\ (\mu-\Lambda)v_+ &= -\frac{1}{2}\nabla^2 v_+ + \lambda(\partial_x + \mathrm{i}\partial_y)v_- \\ &\quad + \mathrm{e}^{r^2}\left(2|\phi_+|^2 + \gamma|\phi_-|^2\right)v_+ \\ &\quad + \mathrm{e}^{r^2}\left(\phi_+^{*2} u_+ + \gamma\phi_+^*\phi_-^* u_- + \gamma\phi_-\phi_+^* v_+\right), \\ (\mu-\Lambda)v_- &= -\frac{1}{2}\nabla^2 v_- - \lambda(\partial_x - \mathrm{i}\partial_y)v_+ \\ &\quad + \mathrm{e}^{r^2}\left(2|\phi_-|^2 + \gamma|\phi_+|^2\right)v_- \\ &\quad + \mathrm{e}^{r^2}\left(\phi_-^{*2} u_- + \gamma\phi_-^*\phi_+^* u_+ + \gamma\phi_+\phi_-^* v_+\right). \end{aligned} \tag{7}$$

This system leads to the eigenvalue problem for the perturbation eigenfrequency, $\Lambda = \Lambda_{\mathrm{r}} + \mathrm{i}\Lambda_{\mathrm{i}}$, written in matrix form:

$$\begin{pmatrix} A_{11} & A_{12} & A_{13} & A_{14} \\ A_{21} & A_{22} & A_{23} & A_{24} \\ A_{31} & A_{32} & A_{33} & A_{34} \\ A_{41} & A_{42} & A_{43} & A_{44} \end{pmatrix} \begin{pmatrix} u_+ \\ u_- \\ v_+ \\ v_- \end{pmatrix} = \Lambda \begin{pmatrix} u_+ \\ u_- \\ v_+ \\ v_- \end{pmatrix}, \tag{8}$$

where the matrix elements are defined as

$$\begin{aligned} A_{11} &= -\frac{1}{2}\nabla^2 - \mu + \mathrm{e}^{r^2}\left(2|\phi_+|^2 + \gamma|\phi_-|^2\right), \\ A_{12} &= \lambda(\partial_x - \mathrm{i}\partial_y) + \mathrm{e}^{r^2}\gamma\phi_-^*\phi_+, \\ A_{13} &= \mathrm{e}^{r^2}\phi_+^2, \quad A_{14} = \mathrm{e}^{r^2}\gamma\phi_+\phi_-, \\ A_{21} &= -\lambda(\partial_x + \mathrm{i}\partial_y) + \mathrm{e}^{r^2}\gamma\phi_+^*\phi_-, \\ A_{22} &= -\frac{1}{2}\nabla^2 - \mu + \mathrm{e}^{r^2}\left(2|\phi_-|^2 + \gamma|\phi_+|^2\right), \\ A_{23} &= A_{14}, \quad A_{24} = \mathrm{e}^{r^2}\phi_-^2, \\ A_{31} &= -A_{13}^*, \quad A_{32} = -A_{23}^*, \\ A_{33} &= -A_{11}^*, \quad A_{34} = -A_{12}^*, \\ A_{41} &= -A_{14}^*, \quad A_{42} = -A_{24}^*, \\ A_{43} &= -A_{21}^*, \quad A_{44} = -A_{22}^*. \end{aligned} \tag{9}$$

The unperturbed solution $\phi_\pm$ is stable if all the eigenvalues Λ are real.

3 Semi-vortex (SV) solitons

3.1 Exact solution

We adopt an ansatz for SV solutions to Eq. (1), with the chemical potential μ, as

$$\begin{aligned} \psi_+(x,y,t) &= \mathrm{e}^{-\mathrm{i}\mu t} f_1(r^2), \\ \psi_-(x,y,t) &= \mathrm{e}^{-\mathrm{i}\mu t + \mathrm{i}\theta} r f_2(r^2), \end{aligned} \tag{10}$$

where (r,θ) are the polar coordinates. The real functions $f_{1,2}(r^2)$ obey the following equations:

$$\begin{aligned} &\mu f_1 + 2(r^2 f_1'' + f_1') - \exp(r^2)\cdot(f_1^2 + \gamma r^2 f_2^2)f_1 \\ &\qquad -2\lambda(r^2 f_2' + f_2) = 0, \\ &\mu f_2 + 2(r^2 f_2'' + 2f_2') - \exp(r^2)\cdot(r^2 f_2^2 + \gamma f_1^2)f_2 \\ &\qquad +2\lambda f_1' = 0, \end{aligned} \tag{11}$$

where

$$f_{1,2}' \equiv \frac{\mathrm{d}}{\mathrm{d}(r^2)} f_{1,2}, \quad f_{1,2}'' \equiv \frac{\mathrm{d}^2}{\mathrm{d}(r^2)^2} f_{1,2}. \tag{12}$$

Further, assuming

$$f_{1,2} = A_\pm \exp(-r^2/2), \tag{13}$$

and substituting this into Eq. (11), it is easy to see that Eqs. (10) and (13) indeed produce an exact solution, provided that the constants are expressed in terms of γ as

follows:

$$\lambda^2 = \frac{(1-\gamma)(2-\gamma)}{4}, \tag{14}$$

$$\mu = \frac{(2-\gamma)}{2(1-\gamma)} + \gamma, \tag{15}$$

$$A_+ = \left[\frac{2-\gamma}{2(1-\gamma)}\right]^{1/2}, \tag{16}$$

$$A_-^2 = 1/2. \tag{17}$$

In particular, Eq. (14) implies that the present exact solution is a particular one (rather than a generic one), because it exists only if the SO coupling strength is adjusted to the value fixed by Eq. (14). According to these results, the norm of each component of the soliton is

$$N_+ = \frac{\pi(2-\gamma)}{2(1-\gamma)}, \tag{18}$$

$$N_- = \frac{\pi}{2}, \tag{19}$$

$$N = N_+ + N_- = \frac{\pi}{2}\left(\frac{2-\gamma}{1-\gamma} + 1\right), \tag{20}$$

and the share of the total norm in the vortical component [see Eq. (5)] is

$$F_- = \frac{1-\gamma}{3-2\gamma}. \tag{21}$$

Equations (14)–(20) suggest that the exact solution is controlled only by γ; moreover, Eq. (14) demonstrates that an exact solution does not exist for $1 \leq \gamma \leq 2$. According to Eqs. (18) and (19), for $0 \leq \gamma < 1$ (where the cross-repulsion is weaker than the self-repulsion), one has $N_+ > N_-$ (the fundamental component is the larger one); however, for $\gamma > 2$, the situation is the opposite and features a larger vortex component: $N_+ < N_-$.

For comparison with the analytical results, we used the numerically obtained solutions for the ground state of the present system generated for the same values of the parameters using the imaginary-time method. The soliton's chemical potential and the norm share of the vortical component, F_- [see Eq. (5)], for $0 \leq \gamma < 1$ and $\gamma > 2$ are compared in Fig. 1. Figures 1(a1, a2) show that the analytical solution produces exactly the ground state for $0 \leq \gamma < 1$. The wave-function profiles produced by the numerical and exact solutions in this case are compared in Figs. 2(a1, a2). Further, Figs. 2(b, c) confirm the stability of the exact solution, which should be expected from the ground state.

However, for $\gamma > 2$, Figs. 1(b1, b2) and 3(a1, a2) show that the analytical and numerical solutions of the ground states are different. In particular, Fig. 1(b2) shows that the numerically found ground state always has $F_- < 0.5$ (i.e., the zero-vorticity component remains the dominant one), whereas the exact solution has $F_- > 0.5$ at $\gamma \geq 2$. Thus, the exact solution represents an excited state of the SV, which is unstable, as seen in Figs. 3(d–f), in contrast to the stability of the numerically found ground state, which is confirmed by Figs. 3(b, c). Finally, the evolution of the norm share in the vortical component, $F_-(t)$, which is displayed in Fig. 3(f), suggests that the evolution of the unstable exact SV at $\gamma > 2$ tends to transform it toward the stable ground state. We note that the full soliton family in the system depends not only on γ, but also on other control parameters, *viz.*, N and λ. Thus, the exact solution produces only specific subfamilies of the solitons, possible links between which are not available in the analytical form. In the following subsection, we produce numerical results for a broader soliton family, into which the analytical branches may be embedded.

3.2 Full numerical results

Numerical forms of the soliton solutions were obtained using the imaginary-time method. To this end, the same

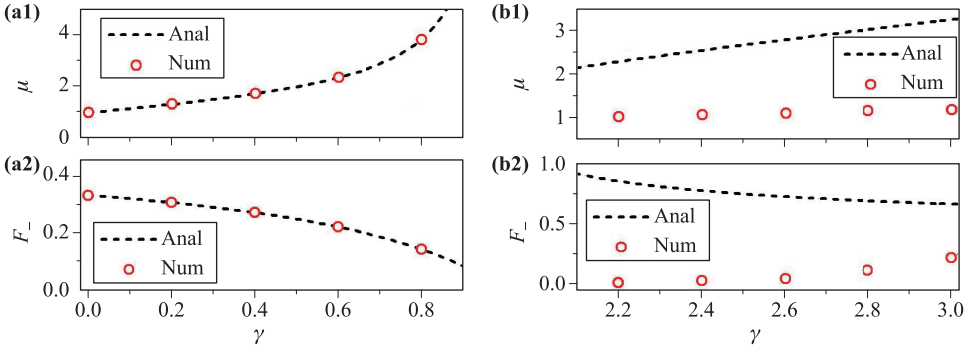

Fig. 1 **(a1, a2)** Comparison between the analytical and numerical results (the black dashed curve and red circles, respectively) for the soliton's chemical potential, μ, and the norm share in the vortical component, F_-, in the region of $0 \leq \gamma < 1$. **(b1, b2)** The same for $\gamma > 2$. Parameters λ (the strength of the SO coupling) and N (the total norm) are here taken as per by Eqs. (14) and (20), respectively. The dashed curves for $\mu(\gamma)$ and $F_-(\gamma)$ are plotted, severally, as per Eqs. (15) and (21).

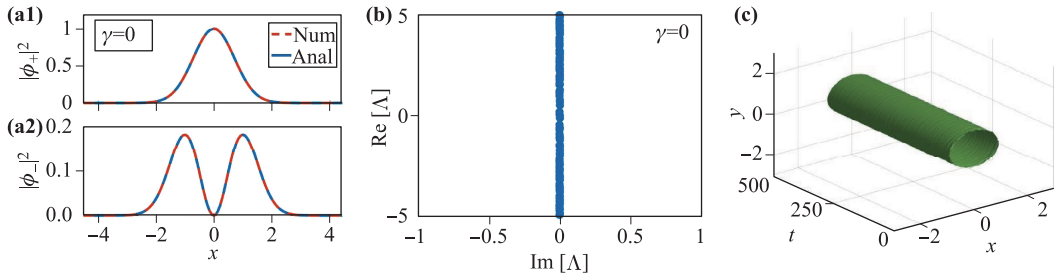

Fig. 2 **(a1, a2)** The comparison between the analytical and numerically found (blue solid and red dashed curves) stationary profiles of the soliton's wave function, shown in cross-section $y = 0$, at $\gamma = 0$. **(b)** Spectra of stability eigenvalues Λ for the exact solution from panels (a1, a2). **(c)** Direct simulations of the evolution of this soliton (with 2% random noise added to the initial conditions), shown by the contour plot of the density profile, $|\psi_+(\boldsymbol{r}, t)|^2$. In this figure, the analytical wave function is taken as per Eqs. (10), (13), (16) and (17), while λ and N are given by Eqs. (14) and (20).

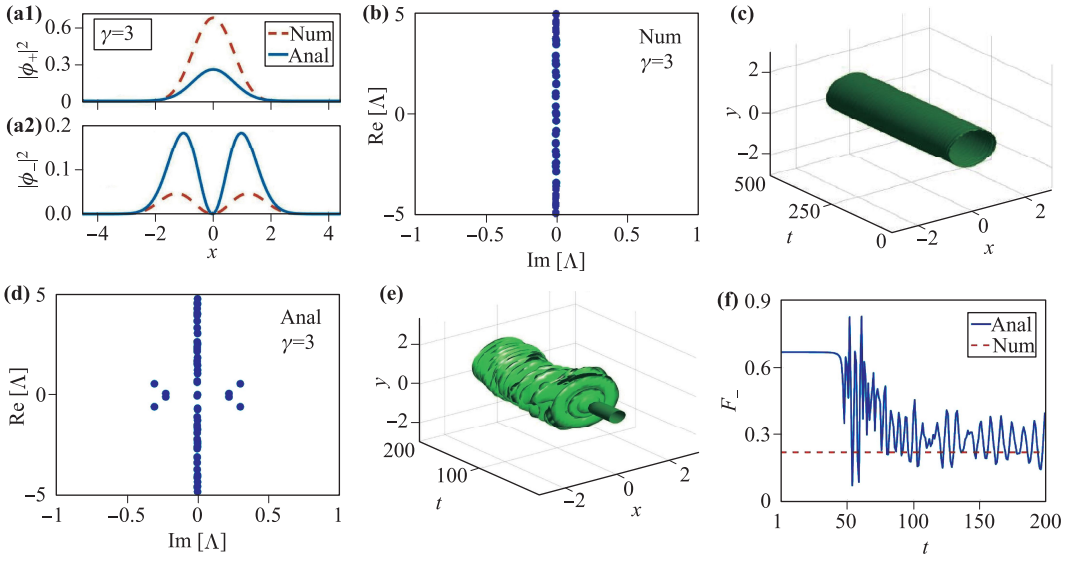

Fig. 3 **(a1, a2)** Comparison between the analytical solution and numerically obtained ground state results (the blue solid and red dashed curves, respectively), shown in cross-section $y = 0$, at $\gamma = 3$. **(b)** Spectra of the stability eigenvalues, Λ, for the numerical solution (the one represented by the red dashed curves in panels (a1, a2). **(c)** Direct simulations to the evolution of the numerical solution (with 2% random noise added to the initial conditions), shown by the contour plot of the density profile, $|\psi_+(\boldsymbol{r}, t)|^2$. **(d)** Spectra of the stability eigenvalues Λ for the analytical solution (represented by the blue solid curve in panels (a1, a2). **(e)** Direct simulations of the perturbed evolution of the analytical solution, shown by the contour plot of the density profile, $|\psi_+(\boldsymbol{r}, t)|^2$. **(f)** F_-, defined as per Eq. (5), as observed in the direct simulations initiated by the exact solution and the numerical one (the blue solid and red dashed curves, respectively). The analytical solution dealt with in this figure is taken as per Eqs. (10), (13), (16) and (17), while parameters λ and N are defined by Eqs. (14) and (20).

input was used as in Ref. [69], which agrees with the general SV ansatz (10):

$$\phi_+^{(0)}(r, \theta) = A_+ \exp(-\alpha_+ r^2),$$
$$\phi_-^{(0)}(r, \theta) = A_- r \exp(\mathrm{i}\theta - \alpha_- r^2), \tag{22}$$

with real constants $A_\pm$ and $\alpha_\pm$. The control parameters are N, γ, and λ.

Figure 4(a) shows the chemical potential of the SV family versus N for different values of γ. The $\mu(N)$ curves exhibit a positive slope, with $\mathrm{d}\mu/\mathrm{d}N > 0$; i.e., they satisfy the anti-Vakhitov–Kolokolov criterion, which is conjectured to provide a necessary stability condition for bright solitons in self-repulsive nonlinear media [83]. SVs with larger values of γ have larger μ, which is also a natural corollary of the repulsive sign of the nonlinearity. The negative slope, $\mathrm{d}\mu/\mathrm{d}\lambda < 0$, in Fig. 4(b) for different values of γ implies that the SO coupling energy is negative and partially compensates for the repulsive nonlinear interactions. The decay of $F_-(N)$ with increasing N observed in Fig. 4(c) shows the same trend as that reported for stable SVs in a self-attractive system [69], i.e., concentration of the norm in the zero-vorticity component. Note that the $F_-(N)$ curves for different values of γ are

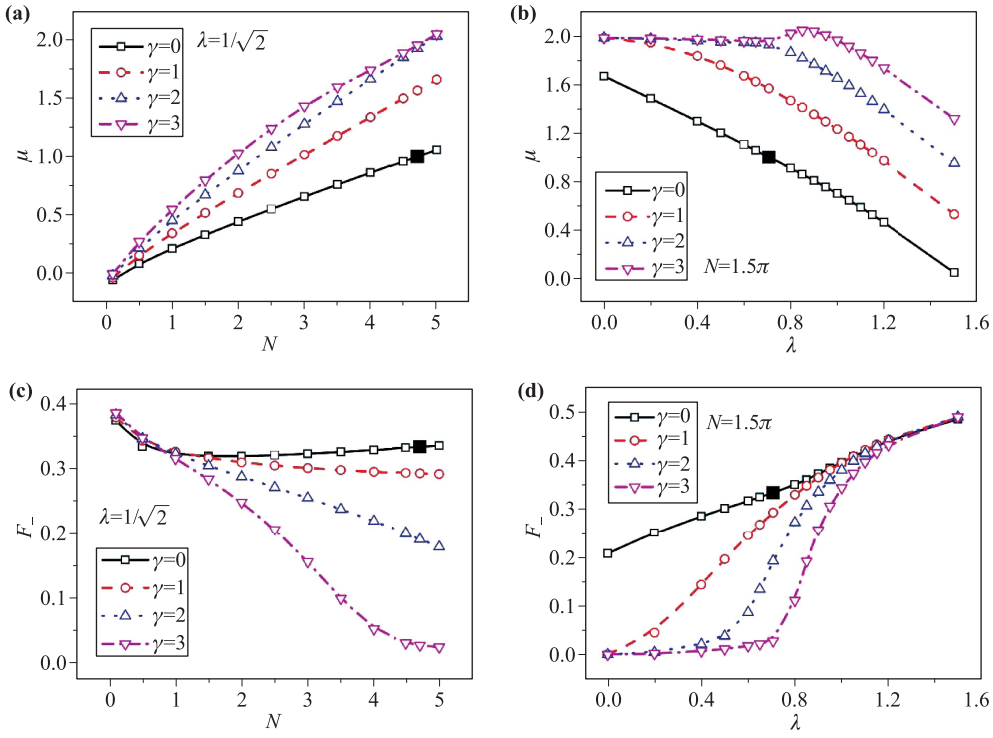

Fig. 4 **(a, b)** The chemical potential of the numerically found family of semi-vortices, μ, versus the total norm, N, and the SO-coupling strength, λ, for different values of the cross/self interaction ratio, $\gamma = 0$, 1, 2, 3, respectively. **(c, d)** The norm share in the vortical component, F_- [see Eq. (5)], versus N and λ for $\gamma = 0$, 1, 2, and 3, respectively. In panels (a, c) and (b, d), $\lambda = 1/\sqrt{2}$ and $N = 1.5\pi$ is fixed, severally. The black solid squares in the panels represent the exact solution, given by Eqs. (10) and (14)–(21), with $\gamma = 0$.

degenerate at small N and split with increasing N, and the vortical component's share, F_-, decays faster under the action of stronger cross-repulsion (for larger γ). On the other hand, Fig. 4(d) demonstrates the growth of F_- with increasing λ, which is also natural, as stronger SO coupling generates more vorticity; i.e., it causes transfer of the norm to the vortical component. In particular, F_- becomes nearly independent of γ at $\lambda > 1$, which means that the SO interaction between the components dominates the nonlinear repulsion between them in this case. In Fig. 4, the exact analytical solutions, which are included in the families of numerically generated ones, are marked by black solid squares.

Finally, we stress that the SV family produced by imaginary-time integration is found to be completely stable (in terms of both the stability eigenvalues and direct simulations) at all values of the parameters, including all values of γ. The latter conclusion is essential because, in the 2D SO-coupled system with attractive interactions, the SVs are stable only at $\gamma \leq 1$ [69].

4 Fundamental mixed-mode (MM) solitons

According to Ref. [69], MM states can be initiated by input that includes terms with vorticities $(0, -1)$ and $(0, +1)$ in the two components,

$$\phi_{\pm}^{(0)}(r,\theta) = A_1 \exp(-\alpha_1 r^2) \mp A_2 r \exp(-\alpha_2 r^2 \mp \mathrm{i}\theta), \quad (23)$$

where $A_{1,2}$ and $\alpha_{1,2}$ are real constants [cf. Eq. (22)]. The initial approximations of the MM states are built as equal-weight superpositions of SVs with topological content $(0, -1)$ and $(0, +1)$ in the two components. In a certain sense, SVs and MMs are similar to immiscible and miscible states, respectively, in binary superfluids. Unlike SVs, MMs cannot be represented by an exact ansatz, but numerical and variational results clearly confirm their existence. A typical example of a stable MM with $(N, \gamma, \lambda) = (2, 0, 1)$, generated by the imaginary-time integration, is shown in Fig. 5.

The numerical analysis demonstrates that, similar to the result reported above for SVs, the family of MM states generated by imaginary-time simulations from input (23) is completely stable at all values of the parameters, including, in particular, all values of γ. This conclusion is essential because, in the 2D SO-coupled system with attractive interactions, MM states are stable only at $\gamma \geq 1$ [69]; i.e., MMs are stable, in the case of attractive nonlinearity, where SVs are not, and vice versa, so they coexist as stable states only in the case of Manakov nonlinearity [84], i.e., at $\gamma = 1$. The stability switch be-

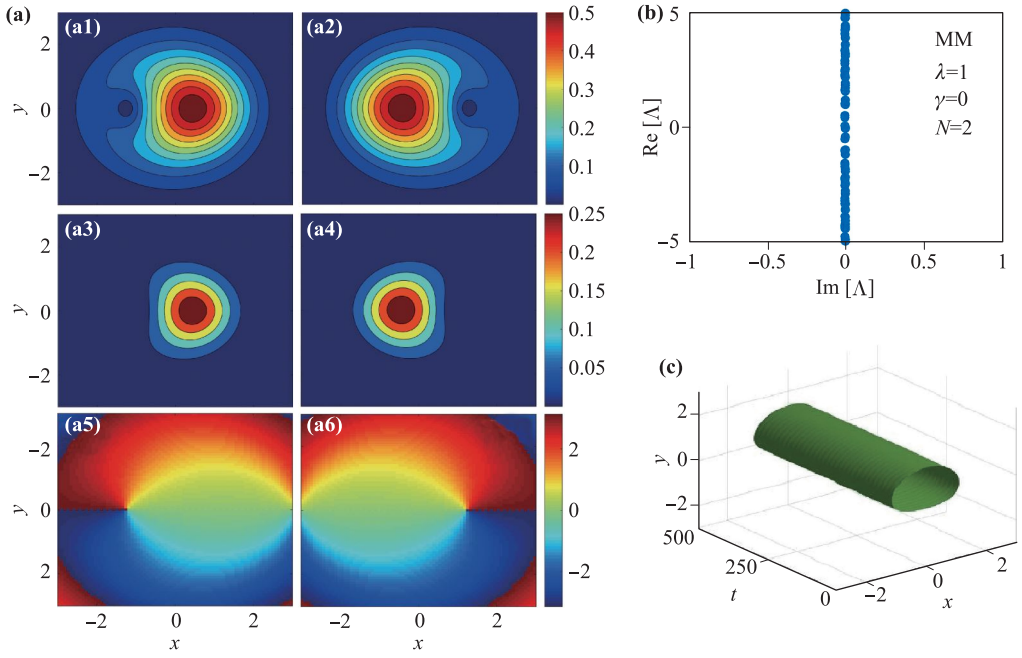

Fig. 5 **(a)** A typical example of a stable MM (mixed-mode) soliton, shown by $|\phi_{\pm}(\boldsymbol{r})|$ (a1, a2), $|\phi_{\pm}(\boldsymbol{r})|^2$ (a3, a4) as well as their phase diagrams (a5, a6), respectively, with $(N, \gamma, \lambda) = (2, 0, 1)$. **(b)** The spectrum of stability eigenvalues for this state. **(c)** Direct simulation of its evolution with 2% noise, shown by means of the density plot, $|\phi_{+}(\boldsymbol{r}, t)|^2$.

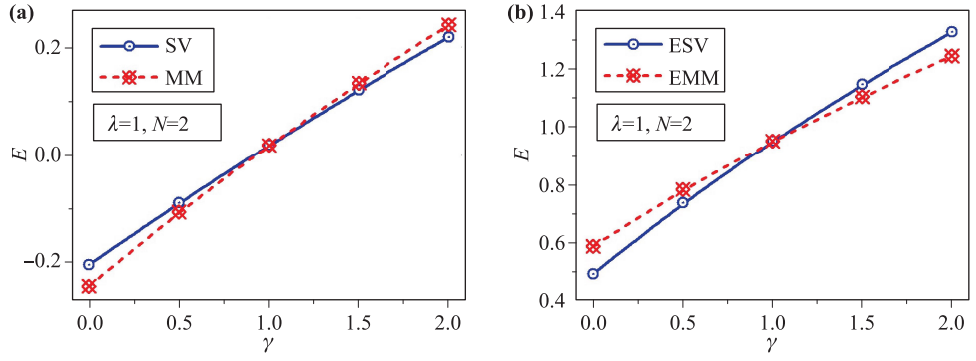

Fig. 6 **(a)** The total energy of the SV (semi-vortex) and MM (mixed-mode) states (blue solid and dashed red curves, respectively) versus γ for a fixed norm, $N = 2$, and a fixed strength of the SO-coupling, $\lambda = 1$. **(b)** The Energy of ESV (excited-state of SV) with $S_+ = 1$ and EMM (Excited state of MM) with $S_1 = 1$ versus γ for fixed $N = 2$ and $\lambda = 1$.

tween SVs and MMs was explained in Ref. [69] by the fact that, for equal values of N, the SV has a lower energy, i.e., it realizes the system's ground state, at $\gamma < 1$, whereas at $\gamma > 1$, the MM provides a lower energy, i.e., the ground state. The SV and MM states are degenerate, having equal energies, at $\gamma = 1$, when both are stable.

In the present system, as noted above, both SVs and MMs are completely stable at all values of γ. This conclusion is natural because the system with repulsive interactions has a definite tendency to be more stable than its attractive counterpart. Nevertheless, it makes sense to identify the ground state of the present system as well by comparing the values of the energy of coexisting SV and MM solitons with equal values of the norm. The comparison is shown in Fig. 6(a), which clearly demonstrates that the SV and MM realize the system's ground state at $\gamma > 1$ and $\gamma < 1$, respectively, which is precisely opposite to the situation in the 2D SO-coupled system with attractive interactions [69]. The same conclusion was obtained for all other values of the parameters, i.e., fixed N and λ.

5 Excited states

Excited states of SVs and MMs are produced by adding extra vorticity to both components of these states. In particular, as suggested by Ref. [69], excited states of SVs

correspond to the following ansatz, which is compatible with Eq. (1) [cf. Eq. (10)]:

$$\psi_+(x,y,t) = \mathrm{e}^{-\mathrm{i}\mu t+\mathrm{i}n\theta} r^n f_1(r^2),$$
$$\psi_-(x,y,t) = \mathrm{e}^{-\mathrm{i}\mu t+\mathrm{i}(n+1)\theta} r^{n+1} f_2(r^2), \tag{24}$$

with $n = 1, 2, \cdots$. However, in the previously studied systems, all the excited states, unlike the fundamental MMs and SVs, were found to be completely unstable in SO-coupled systems with homogeneous contact nonlinearities [69, 85]. Very recently, stable excited states of SVs and MMs were predicted in a model of a 2D dipolar BEC with long-range interactions between field-induced dipoles whose magnitude grows from the center to the periphery [86]. The latter finding motivates exploration of the existence and stability of excited states in the present system with contact repulsive interactions.

We performed the analysis, running imaginary-time simulations using the following inputs for the excited states of SVs:

$$\phi_\pm^{(0)} = A_\pm r^{|S_\pm|} \exp(-\alpha_\pm r^2 + \mathrm{i}S_\pm\theta) \tag{25}$$

[cf. the general exact ansatz (24)] and for the excited states of MMs:

$$\phi_\pm^{(0)} = A_1 r^{|S_1|} \exp(-\alpha_1 r^2 \pm \mathrm{i}S_1\theta)$$
$$\mp A_2 r^{|S_2|} \exp(-\alpha_2 r^2 \mp \mathrm{i}S_2\theta), \tag{26}$$

where $A_\pm$, $A_{1,2}$, $\alpha_\pm$, and $\alpha_{1,2}$ are real constants; $S_{+,1} = 0, \pm1, \pm2, \cdots$ are integers, and $S_{-,2} = S_{+,1} + 1$. In Eq. (25), fundamental SVs are produced by $(S_+, S_-) = (-1, 0)$ or $(0, 1)$ [cf. Eq. (22)], and their excited states correspond to $(S_+, S_-) = (n, n+1)$, where $n \neq -1$ or 0. Similarly, Eq. (26) produces fundamental MMs for $S_1 = -1$ and 0, and their excited states correspond to other integer values of S_1. Below, we fix $\lambda = 1$ and consider $S_{+,1} \geq 1$ for $N \leq 5$ and $\gamma \leq 2$.

The numerical results demonstrate that embedded states of SVs may be stable up to $S_+ = 5$, whereas MMs in the excited states are stable only up to $S_1 = 2$. Examples of the 2D excited states are displayed in Fig. 7. The SVs feature a standard ring structure in each component (see top three rows in Fig. 7), where the topo-

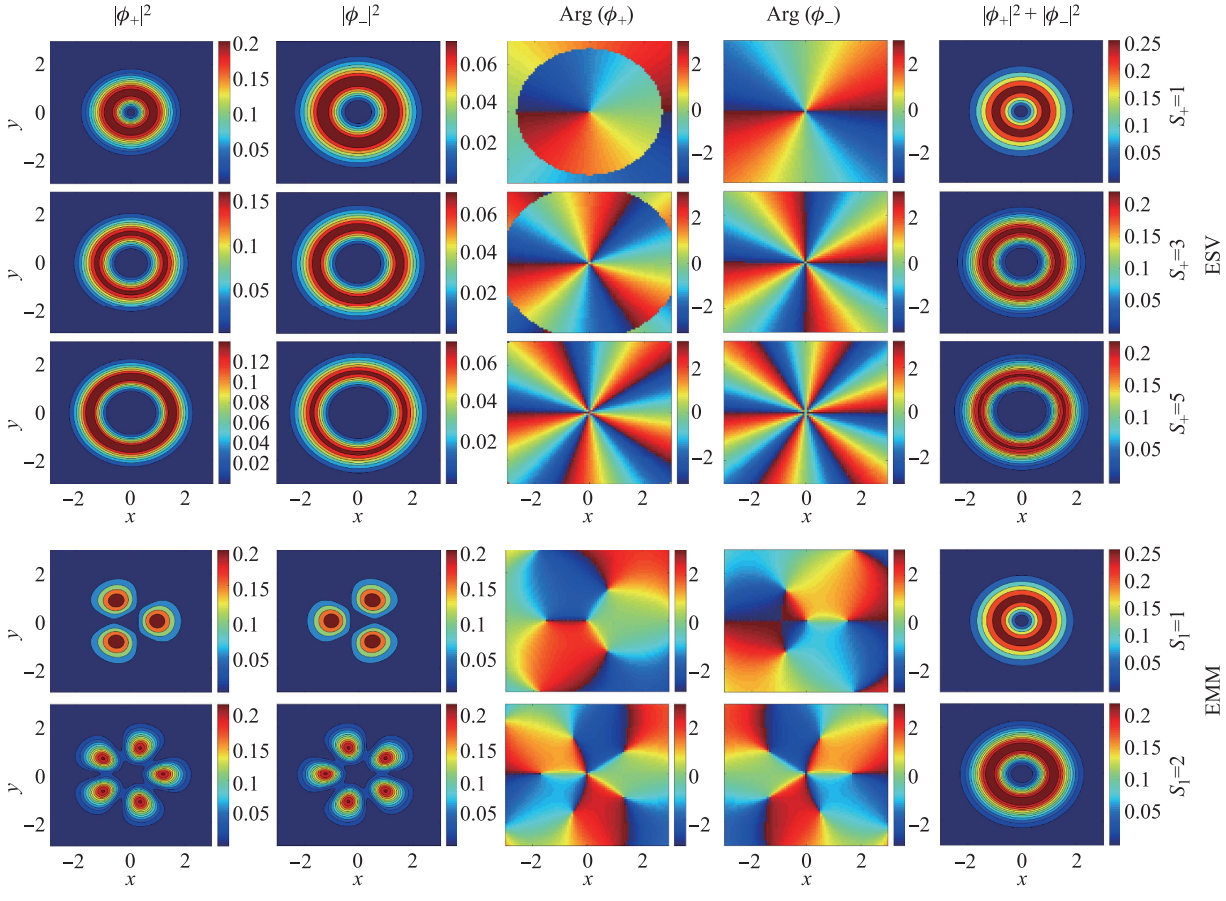

Fig. 7 Examples of stable excited states of SVs ("ESVs") with $S_+ = 1$, 3, and 5 (the first, second, and third rows, respectively), and of MMs ("EMMs") with $S_1 = 1$ and 2 (the fourth and fifth rows, respectively). The first and second columns display density patterns of components $\phi_\pm$, while the third and fourth columns display phase structures of $\phi_\pm$. The fifth column is the total-density pattern, $n(\boldsymbol{r}) = |\phi_+|^2 + |\phi_-|^2$. Parameters are $N = 2$, $\gamma = 1$ and $\lambda = 1$ for all the panels.

logical charges are identical to the values of $S_\pm$ in the input [Eq. (25)]. For the MMs, each component of the excited state is built as an annular necklace structure, and the number of fragments in the necklaces is exactly equal to $S_1 + S_2 = 2S_1 + 1$; see the bottom two rows in Fig. 7. The total angular momentum of the MM states is $L = (L_+ + L_-)/2 \equiv 0$. The total density, i.e., $|\phi_+(\boldsymbol{r})|^2 + |\phi_-(\boldsymbol{r})|^2$, of the excited states of both SVs and MMs exhibits perfect ring patterns. The dependence of the necklace pattern of the excited MM states on the SO strength, λ, is illustrated in Fig. 8, which displays excited MMs with $(N, \gamma) = (2, 1)$ and different values of λ. The figure shows that the main density pattern of the excited MM states shrinks with increasing λ, and higher-order lobes emerge from the pattern's core. Somewhat similar 2D necklace patterns were realized recently in an SO-coupled BEC in an annular trapping potential [87, 88], where they are ground states and exhibit a λ dependence different from that of those produced by the excited MM states in the current work.

Typical examples of the evolution of stable and unstable excited states are displayed in Fig. 9. As mentioned above, excited states of SVs are stable for $S_+ \leq 5$. At $S_+ > 5$, the instability perturbs the SV pattern but does not destroy its vortex structure. Excited states of MMs are stable only for $S_1 = 1$ and 2. Unstable MM excited states tend to change into fundamental MMs.

The different instability evolution of SV and MM excited states is explained by the presence of angular momentum in SVs. As a result, unstable excited states of SVs maintain the initial value of the angular momentum, which prevents their transformation into their stable counterparts with smaller values of the angular momentum [see an example in Figs. 9(b, c), where the output phase pattern demonstrates that the vorticity of ψ_+ remains 6]. On the other hand, the zero total angular momentum of unstable MM excited states allows them to simplify themselves into the fundamental MM; see the example in Figs. 9(e, f).

Finally, families of excited states of SVs and MMs are

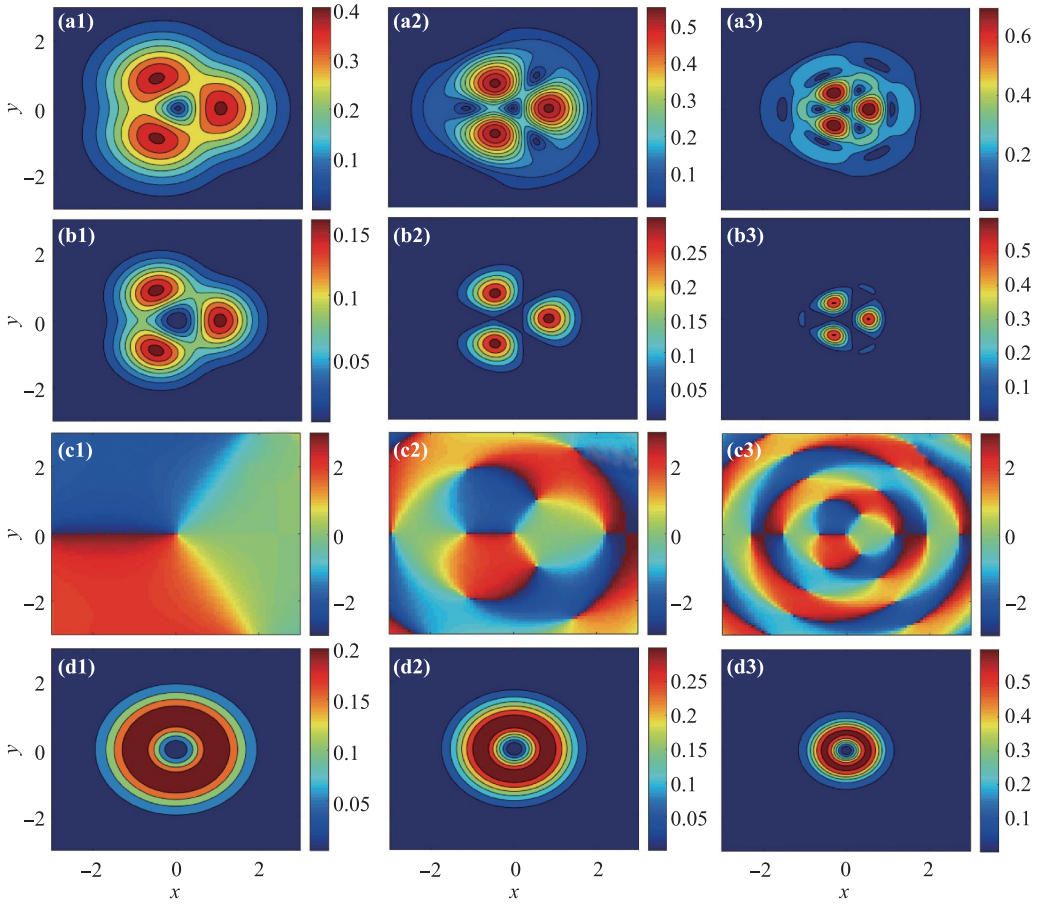

Fig. 8 **(a1–a3)** $|\phi_+|$ with $\lambda = 0.2$ (a1), 2 (a2) and 4 (a3). **(b1–b3)** $|\phi_+|^2$ with $\lambda = 0.2$ (b1), 2 (b2) and 4 (b3). **(c1–c3)** The phase diagram of ϕ_+ with $\lambda = 0.2$ (c1), 2 (c2) and 4 (c3). **(d1–d3)** Total density pattern $n(\boldsymbol{r}) = |\phi_+(\boldsymbol{r})|^2 + |\phi_-(\boldsymbol{r})|^2$ with $\lambda = 0.2$ (d1), 2 (d2) and 4 (d3). Total norm and γ of these examples are fixed by $(N, \gamma) = (2, 1)$. Solitons in these panels are all stable.

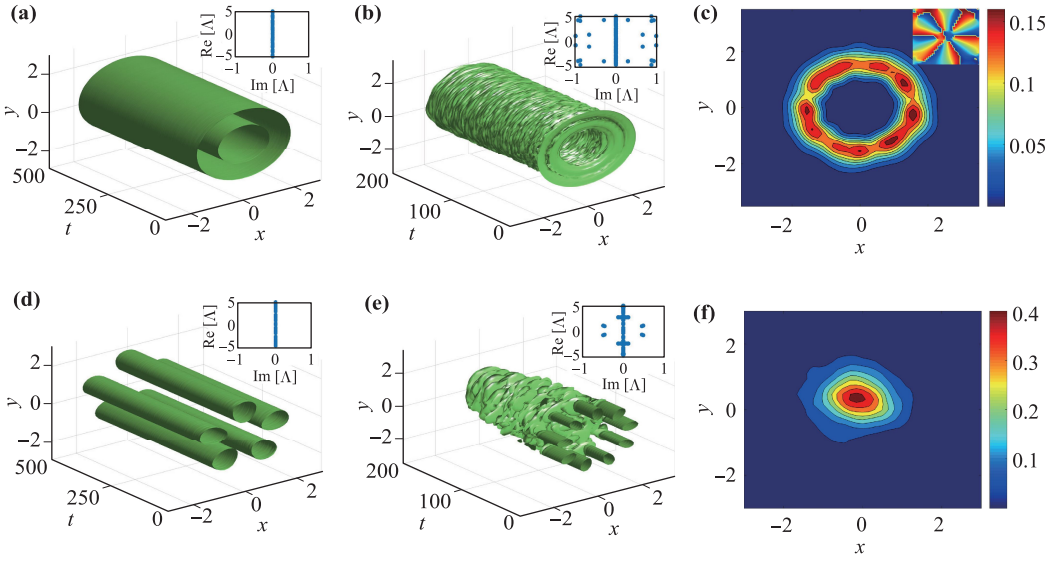

Fig. 9 Example of the real-time evolution of stable and unstable excited states of SVs and MMs. **(a)** A stable SV's excited state with $(N, \gamma, \lambda, S_+) = (2, 1, 1, 4)$. **(b)** An unstable SV state with $(N, \gamma, \lambda, S_+) = (2, 1, 1, 6)$. **(c)** The final density pattern of $|\psi_+|^2$, corresponding to panel (b), the inset showing the respective phase pattern. **(d)** A stable excited state of the MM with $(N, \gamma, \lambda, S_1) = (2, 1, 1, 2)$. **(e)** An unstable MM state with $(N, \gamma, \lambda, S_1) = (2, 1, 1, 4)$. **(f)** The final density pattern of $|\psi_+|^2$, corresponding to panel (e). Spectra of stability eigenvalues for these modes are shown as insets in panels (a), (b), (d) and (e).

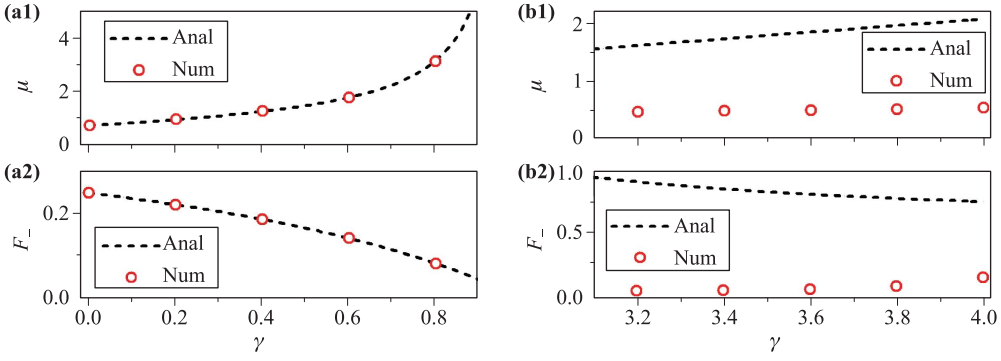

Fig. 10 **(a1, a2)** The comparison between the exact analytical result (the black dashed curve) and numerical findings, produced by the imaginary-time simulations of the 1D system (red circles) for μ and F_- in the region of $0 \leq \gamma < 1$. **(b1, b2)** The same at $\gamma > 3$. Parameters λ (the strength of the SO coupling) and N (the total norm) are defined by Eqs. (32) and (38), respectively. The analytical expressions for $\mu(\gamma)$ and $F_-(\gamma)$ are given by Eqs. (33) and (39), respectively.

characterized by the corresponding $E(\gamma)$ dependence, as shown in Fig. 6(b) with fixed values of S_+ and S_1 for $N = 2$. This panel shows that the first excited states of SVs and MMs are degenerate, having equal energies, at $\gamma = 1$. The SV excited states have a lower energy than their counterparts of the MM type at $\gamma < 1$, and vice versa at $\gamma > 1$.

6 Soliton in the 1D model

The 1D reduction of the 2D system (1) is described by the following system of coupled GPEs:

$$i\partial_t \psi_\pm = -\frac{1}{2}\partial_{xx}^2 \psi_\pm + \exp(+x^2)\cdot(|\psi_\pm|^2 + \gamma|\psi_\mp|^2)\psi_\pm \pm \lambda \partial_x \psi_\mp. \tag{27}$$

Stationary solutions with chemical potential are searched for in the usual form, $\psi_\pm(x,t) = \mathrm{e}^{-\mathrm{i}\mu t} u_\pm(x)$, where real functions $u_\pm(x)$ (unlike the complex stationary wave function in the 2D case) solve the equations

$$\mu u_+ + \frac{1}{2}u_+'' - \mathrm{e}^{x^2}(u_+^2 + \gamma u_-^2)u_+ - \lambda u_-' = 0, \tag{28}$$

$$\mu u_- + \frac{1}{2}u_-'' - \mathrm{e}^{x^2}(u_-^2 + \gamma u_+^2)u_- + \lambda u_+' = 0, \tag{29}$$

where the prime symbol stands for $\mathrm{d}/\mathrm{d}x$. A particular

exact solution to Eqs. (28) and (29) with one even and one odd component, which may be considered to be a 1D counterpart of the 2D SV states, is searched for in the form of

$$u_+ = A_+ \exp(-x^2/2), \quad u_- = A_- x \exp(-x^2/2). \quad (30)$$

Equation (30) implies that the component u_- has a dipole structure; therefore, modes of this type may be called semi-dipole solitons. Substituting this component into Eqs. (28) and (29), we obtain the following relations between the constants:

$$\begin{aligned} &\mu A_+ - \frac{1}{2}A_+ - A_+^3 - \lambda A_- = 0, \\ &\frac{A_+}{2} - \gamma A_-^2 A_+ + \lambda A_- = 0, \\ &\mu A_- - \frac{3}{2}A_- - \gamma A_+^2 A_- - \lambda A_+ = 0, \\ &\frac{1}{2}A_- - A_-^3 = 0. \end{aligned} \quad (31)$$

Solving Eq. (31) yields

$$\lambda^2 = \frac{(\gamma-1)(\gamma-3)}{8}, \quad (32)$$

$$\mu = \frac{(\gamma+1)(2\gamma-3)}{4(\gamma-1)}, \quad (33)$$

$$A_+^2 = \frac{(\gamma-3)}{4(\gamma-1)}, \quad (34)$$

$$A_-^2 = \frac{1}{2}. \quad (35)$$

Equation (32) indicates that exact solutions exist for $\gamma < 1$ and $\gamma > 3$. The norms of the two components of the exact solution are

$$N_+ = \frac{\sqrt{\pi}}{4}\left(\frac{\gamma-3}{\gamma-1}\right), \quad (36)$$

$$N_- = \frac{\sqrt{\pi}}{4}, \quad (37)$$

$$N = N_+ + N_- = \frac{\sqrt{\pi}}{2}\left(\frac{\gamma-2}{\gamma-1}\right). \quad (38)$$

Therefore, the 1D version of the analytical result for the relative share of the total norm that is kept in the odd component is

$$F_- = \frac{\gamma-1}{2(\gamma-2)} \quad (39)$$

[cf. Eq. (5)]. Like those of the exact 2D solution, the parameters of the 1D solution, λ and N, are defined only by γ [cf. Eqs. (14) and (20)]. Moreover, according to Eq. (39), if $0 \le \gamma < 1$, then $F_- < 0.5$ (the fundamental component is the larger one); however, if $\gamma > 3$, then $F_- > 0.5$ (the vortex component is larger).

Figure 10 compares the analytical solution and the numerical results, which were produced by imaginary-time integration of Eq. (27), for μ and F_- in the regions $0 \le \gamma < 1$ and $\gamma > 3$. Similar to the situation for the 2D system (Fig. 1), for $0 \le \gamma < 1$, the analytical solution exactly produces the ground state, whereas at $\gamma > 3$, the analytical solution corresponds to some excited state, and the ground state is very different. The corresponding wave functions produced by the numerical and exact solutions for $0 \le \gamma < 1$ and $\gamma > 3$ are compared in Figs. 11(a1, a2) and 12(a1, a2), respectively.

The stability of the analytical and numerical solutions was verified by numerical computation of the respective eigenvalues and through direct simulations of Eq. (27). Again, as in the 2D case, the simulations show that the analytical exact solution and its numerical counterpart are completely stable for $0 \le \gamma < 1$; see a typical example for $\gamma = 0.5$ in Fig. 11. On the other hand, for $\gamma > 3$, the numerical solution is stable, whereas the exact one is not. Typical examples of the stable and unstable evolution of $\gamma = 3.5$ are displayed in Fig. 12.

According to the patterns of the analysis presented in Section 3.2, families of generic semi-dipole states can be found using the imaginary-time method as applied to Eq. (27) with the input taken according to Eq. (30). As in Fig. 4, we characterize the semi-dipole families by plotting μ and F_- versus N and λ in Fig. 13. The exact

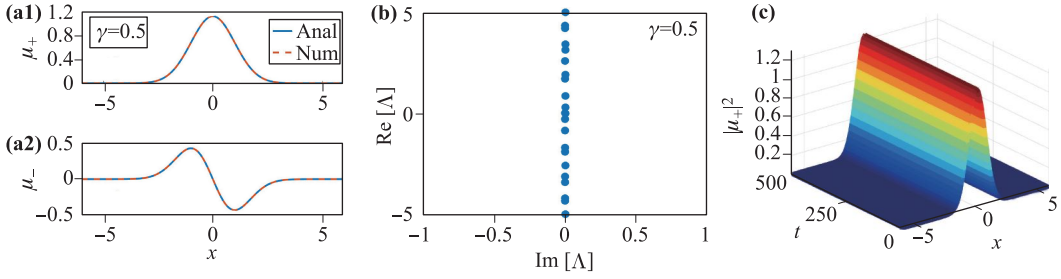

Fig. 11 **(a1, a2)** The comparison between the analytical and numerical results (the blue solid and red dashed curves) for the 1D wave function with $\gamma = 0.5$. **(b)** The spectrum of stability eigenvalues Λ for the exact solution from panels (a1, a2). **(c)** Direct simulations of the evolution of this soliton. Here the analytical wave functions are given by Eqs. (30), (34) and (35), while λ and N are defined by Eqs. (32) and (38), respectively.

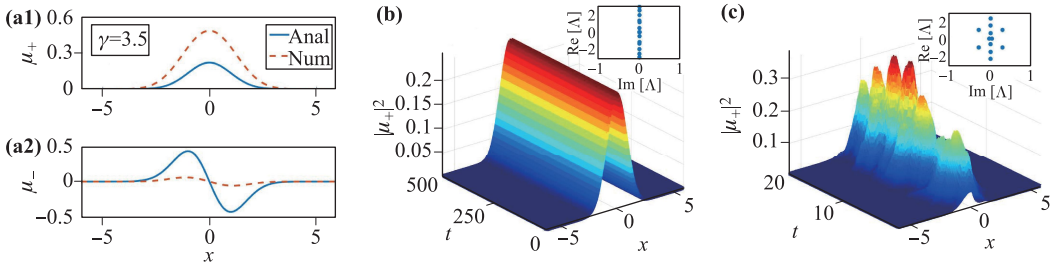

Fig. 12 **(a1, a2)** Comparison between the analytical and numerically found (the blue solid and red dashed curves, respectively) for the 1D soliton wave function at $\gamma = 3.5$. **(b, c)** Direct simulations to the evolution initiated by the numerical and analytical solution, respectively. Insets arespectra of stability eigenvalues Λ for them. Here the analytical wave functions are defined by Eqs. (30), (34) and (35), while λ and N are defined by Eqs. (32) and (38), respectively.

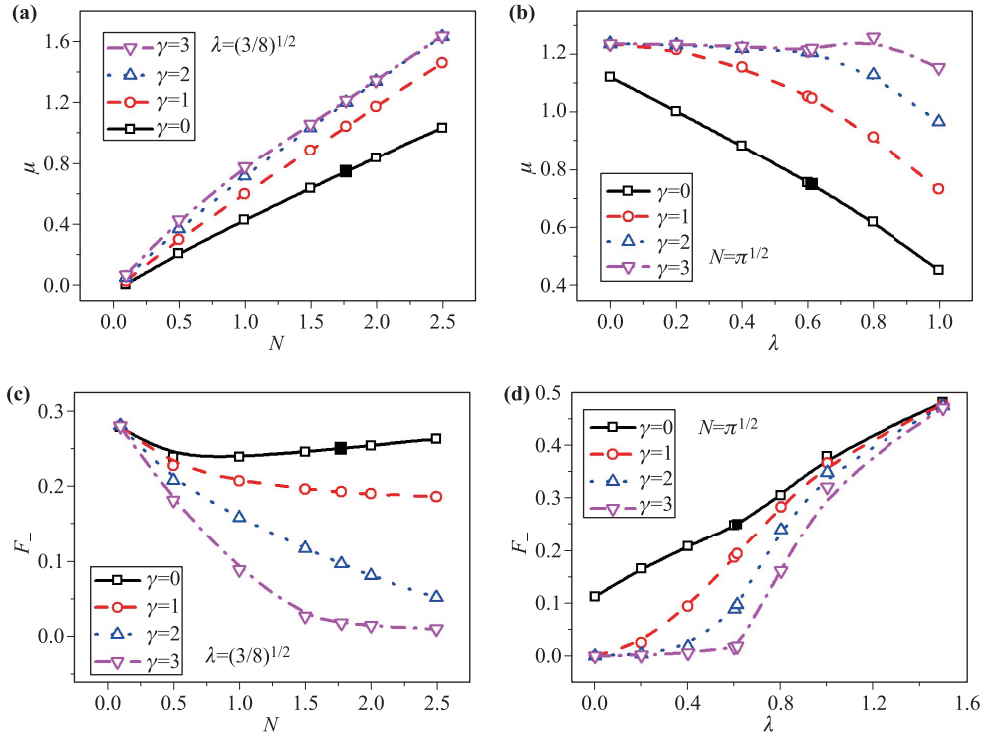

Fig. 13 The chemical potential of the numerically found family of 1D semi-vortices, μ, versus the total norm, N, and the SO-coupling strength, λ, for different values of the cross/self interaction ratio, $\gamma = 0$, 1, 2, 3, respectively. **(c, d)** The norm share in the vortical component, F_- [see Eq. (39)], versus N and λ for $\gamma = 0$, 1, 2, and 3, respectively. In panels **(a, c)** and **(b, d)**, $\lambda = \sqrt{3/8}$ and $N = \sqrt{\pi}$ is fixed, severally. The black solid squares in the panels represent the exact solution, given by Eqs. (30)–(39), with $\gamma = 0$.

analytical solution given by Eqs. (30) and (32)–(39) is included in the figure.

Further, the 1D version of MMs can also be found in numerical form starting from the ansatz

$$u_{\pm} = (A_1 \pm A_2 x)\exp(-x^2/2). \tag{40}$$

A typical example, the stable 1D MM for $\gamma = 0$, is displayed in Fig. 14. The $E(\gamma)$ curves for the 1D semi-dipoles and MMs are shown in Fig. 14(c) and demonstrate that these two species of 1D solitons are almost degenerate in terms of the energy.

7 Conclusion

The objective of this work was to construct 2D solitons in SO-coupled two-component BECs with contact repulsive interactions whose local strength grows from the center to the periphery sufficiently rapidly. By using the anti-Gaussian modulation profile, exact analytical solutions

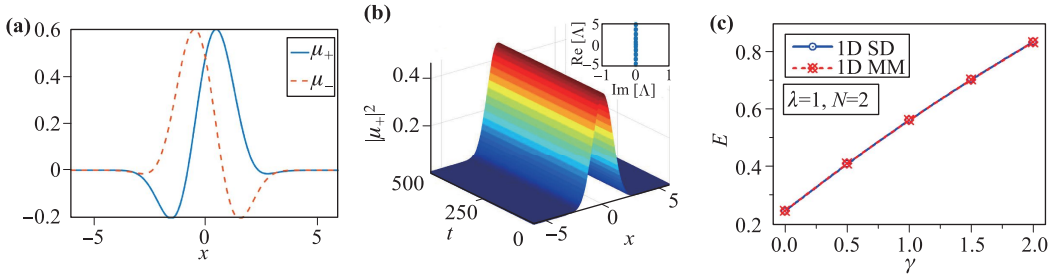

Fig. 14 **(a, b)** A typical example of numerically found stable 1D mixed-mode solitons with $(N, \gamma, \lambda) = (2, 0, 1)$. **(c)** Energies of the 1D semi-dipole and MM solitons versus γ for fixed $N = 2$ and $\lambda = 1$.

of the SV type were found. These solutions are controlled chiefly by the relative strength of the cross repulsion, γ. Exact solutions exist for $\gamma < 1$ and $\gamma > 2$. Numerical results demonstrated that the exact solutions are stable ground states at $\gamma < 1$, whereas at $\gamma > 2$, they are unstable excited modes, and the ground state has a different solution, which is found in numerical form. Other types of 2D solitons, *viz.*, fundamental MMs and excited states of SVs and MMs, are found numerically, as well as the full family of SVs, in which the exact analytical solutions are included as particular ones. All the fundamental solutions of both the SV and MM types are completely stable. They are identified as the ground state at $\gamma > 1$ and $\gamma < 1$, respectively, and their excited states, which are produced by adding the vorticity S to both components, are partially stable up to $S = 5$ and 2 for SVs and MMs, respectively. The 1D reduction of the system was also considered. In particular, exact states in the form of semi-dipoles, which are 1D counterparts of SVs, were found at $\gamma < 1$. Families of generic 1D solitons of the semi-dipole and MM types were found in numerical form. These two types of 1D solitons are close to being mutually degenerate, as they have almost equal energies.

The present analysis can be further extended. First, a natural possibility is to explore the SO-coupled system with a mixture of Rashba and Dresselhaus coupling terms. Next, one can consider the limit case of strong SO coupling, which makes it possible to neglect the kinetic energy terms in Eq. (1) and thus replace it by a nonlinear Dirac/Weyl model. Finally, a challenging option is to seek extension of the current setting to the 3D geometry.

Acknowledgements This work was supported in part by the National Natural Science Foundation of China through Grant Nos. 11575063, 61471123, and 61575041, the Joint Program in Physics of the NSF and the Binational (US-Israel) Science Foundation through Project No. 2015616, the Israel Science Foundation (project No. 1287/17), and the Natural Science Foundation of Guangdong Province through Grant No. 2015A030313639. B.A.M. is grateful for a foreign-expert grant from Guangdong province (China) and a Ding-Ying professorship provided by the South China Agricultural University (Guangzhou) at its College of Electronic Engineering.

References

1. L. Bergé, Wave collapse in physics: Principles and applications to light and plasma waves, *Phys. Rep.* 303(5–6), 259 (1998)
2. G. Fibich and G. Papanicolaou, Self-focusing in the perturbed and unperturbed nonlinear Schrödinger equation in critical dimension, *SIAM J. Appl. Math.* 60(1), 183 (1999)
3. A. S. Desyatnikov, L. Torner, and Y. S. Kivshar, Optical vortices and vortex solitons, *Prog. Opt.* 47, 291 (2005)
4. B. A. Malomed, D. Mihalache, F. Wise, and L. Torner, Spatiotemporal optical solitons, *J. Optics B: Quant. Semicl. Opt.* 7(5), R53 (2005)
5. B. Malomed, L. Torner, F. Wise, and D. Mihalache, Viewpoint: On multidimensional solitons and their legacy in contemporary Atomic, Molecular and Optical physics, *J. Phys.: At. Mol. Opt. Phys.* 49(17), 170502 (2016)
6. D. Mihalache, Multidimensional localized structures in optics and Bose–Einstein condensates: A selection of recent studies, *Rom. J. Phys.* 59, 295 (2014)
7. B. A. Malomed, Multidimensional solitons: Well-established results and novel findings, *Eur. Phys. J. Spec. Top.* 225(13–14), 2507 (2016)
8. V. S. Bagnato, D. J. Frantzeskakis, P. G. Kevrekidis, B. A. Malomed, and D. Mihalache, Bose–Einstein condensation: Twenty years after, *Rom. Rep. Phys.* 67, 5 (2015)
9. D. Mihalache, Multidimensional localized structures in optical and matter-wave media: A topical survey of recent literature, *Rom. Rep. Phys.* 69, 403 (2017)
10. J. Zeng and B. A. Malomed, Localized dark solitons and vortices in defocusing media with spatially inhomogeneous nonlinearity, *Phys. Rev. E* 95, 052214 (2017)
11. X. Gao and J. Zeng, Two-dimensional matter-wave solitons and vortices in competing cubic-quintic nonlinear lattices, *Front. Phys.* 13(1), 130501 (2018)

12. O. V. Borovkova, Y. V. Kartashov, B. A. Malomed, and L. Torner, Algebraic bright and vortex solitons in defocusing media, *Opt. Lett.* 36(16), 3088 (2011)
13. O. V. Borovkova, Y. V. Kartashov, L. Torner, and B. A. Malomed, Bright solitons from defocusing nonlinearities, *Phys. Rev. E* 84, 035602(R) (2011)
14. Y. V. Kartashov, V. A. Vysloukh, L. Torner, and B. A. Malomed, Self-trapping and splitting of bright vector solitons under inhomogeneous defocusing nonlinearities, *Opt. Lett.* 36(23), 4587 (2011)
15. V. E. Lobanov, O. V. Borovkova, Y. V. Kartashov, B. A. Malomed, and L. Torner, Stable bright and vortex solitons in photonic crystal fibers with inhomogeneous defocusing nonlinearity, *Opt. Lett.* 37(11), 1799 (2012)
16. Q. Tian, L. Wu, Y. Zhang, and J. F. Zhang, Vortex solitons in defocusing media with spatially inhomogeneous nonlinearity, *Phys. Rev. E* 85(5), 056603 (2012)
17. Y. Wu, Q. Xie, H. Zhong, L. Wen, and W. Hai, Algebraic bright and vortex solitons in self-defocusing media with spatially inhomogeneous nonlinearity, *Phys. Rev. A* 87(5), 055801 (2013)
18. R. Driben, Y. V. Kartashov, B. A. Malomed, T. Meier, and L. Torner, Soliton gyroscopes in media with spatially growing repulsive nonlinearity, *Phys. Rev. Lett.* 112(2), 020404 (2014)
19. Y. V. Kartashov, B. A. Malomed, Y. Shnir, and L. Torner, Twisted toroidal vortex-solitons in inhomogeneous media with repulsive nonlinearity, *Phys. Rev. Lett.* 113(26), 264101 (2014)
20. R. Driben, Y. Kartashov, B. A. Malomed, T. Meier, and L. Torner, Three-dimensional hybrid vortex solitons, *New J. Phys.* 16(6), 063035 (2014)
21. J. Hukriede, D. Runde, and D. Kip, Fabrication and application of holographic Bragg gratings in lithium niobate channel waveguides, *J. Phys. D* 36(3), R1 (2003)
22. G. Roati, M. Zaccanti, C. D'Errico, J. Catani, M. Modugno, A. Simoni, M. Inguscio, and G. Modugno, ^{39}K Bose–Einstein condensate with tunable interactions, *Phys. Rev. Lett.* 99(1), 010403 (2007)
23. S. E. Pollack, D. Dries, M. Junker, Y. P. Chen, T. A. Corcovilos, and R. G. Hulet, Extreme tunability of interactions in a ^{7}Li Bose–Einstein condensate, *Phys. Rev. Lett.* 102(9), 090402 (2009)
24. F. K. Abdullaev, A. Gammal, and L. Tomio, Dynamics of bright matter-wave solitons in a Bose–Einstein condensate with inhomogeneous scattering length, *J. Phys.: At. Mol. Opt. Phys.* 37(3), 635 (2004)
25. L. W. Clark, L. C. Ha, C. Y. Xu, and C. Chin, Quantum dynamics with spatiotemporal control of interactions in a stable Bose–Einstein condensate, *Phys. Rev. Lett.* 115(15), 155301 (2015)
26. R. Yamazaki, S. Taie, S. Sugawa, and Y. Takahashi, Quantum dynamics with spatiotemporal control of interactions in a stable Bose–Einstein condensate, *Phys. Rev. Lett.* 105, 050405 (2010)
27. M. Yan, B. J. DeSalvo, B. Ramachandhran, H. Pu, and T. C. Killian, Controlling condensate collapse and expansion with an optical Feshbach resonance, *Phys. Rev. Lett.* 110(12), 123201 (2013)
28. D. M. Bauer, M. Lettner, C. Vo, G. Rempe, and S. Dürr, Control of a magnetic Feshbach resonance with laser light, *Nat. Phys.* 5(5), 339 (2009)
29. Y. Li, J. Liu, W. Pang, and B. A. Malomed, Matter-wave solitons supported by field-induced dipole-dipole repulsion with spatially modulated strength, *Phys. Rev. A* 88(5), 053630 (2013)
30. F. Kh. Abdullaev, A. Gammal, B. A. Malomed, and L. Tomio, Bright solitons in Bose–Einstein condensates with fieldinduced dipole moments, *J. Phys. B* 47(7), 075301 (2014)
31. Y. Li, Z. Fan, Z. Luo, Y. Liu, H. He, J. Lü, J. Xie, C. Huang, and H. Tan, Cross-symmetry breaking of two-component discrete dipolar matter-wave solitons, *Front. Phys.* 12, 124206 (2017)
32. X. Chen, Y. Chuang, C. Lin, C. Wu, Y. Li, B. A. Malomed, and R. Lee, Magic tilt angle for stabilizing two-dimensional solitons by dipole-dipole interactions, *Phys. Rev. A* 96, 043631 (2017)
33. Y. Li, W. Pang, J. Xu, C. Lee, B. A. Malomed, and L. Santos, Long-range transverse Ising model built with dipolar condensates in two-well arrays, *New J. Phys.* 19(1), 013030 (2017)
34. Y. J. Lin, K. Jimenez-Garcia, and I. B. Spielman, Spin-orbit-coupled Bose–Einstein condensates, *Nature* 471(7336), 83 (2011)
35. D. L. Campbell, G. Juzeliūnas, and I. B. Spielman, Realistic Rashba and Dresselhaus spin-orbit coupling for neutral atoms, *Phys. Rev. A* 84(2), 025602 (2011)
36. Y. Zhang, L. Mao, and C. Zhang, Mean-field dynamics of spin-orbit coupled Bose–Einstein condensates, *Phys. Rev. Lett.* 108(3), 035302 (2012)
37. V. Galitski and I. B. Spielman, Spin-orbit coupling in quantum gases, *Nature* 494(7435), 49 (2013)
38. H. Zhai, Degenerate quantum gases with spin-orbit coupling: A review, *Rep. Prog. Phys.* 78(2), 026001 (2015)
39. Z. Wu, L. Zhang, W. Sun, X. T. Xu, B. Z. Wang, S. C. Ji, Y. Deng, S. Chen, X. J. Liu, and J. W. Pan, Realization of two-dimensional spin-orbit coupling for Bose–Einstein condensates, *Science* 354(6308), 83 (2016)
40. Z. Meng, L. Huang, P. Peng, D. Li, L. Chen, Y. Xu, C. Zhang, P. Wang, and J. Zhang, Experimental observation of a topological band gap opening in ultracold Fermi gases with two-dimensional spin-orbit coupling, *Phys. Rev. Lett.* 117(23), 235304 (2016)
41. Y. Zhang, M. E. Mossman, T. Busch, P. Engels, and C. Zhang, Properties of spin-orbit-coupled Bose–Einstein condensates, *Front. Phys.* 11(3), 118103 (2016)
42. C. Wang, C. Gao, C. M. Jian, and H. Zhai, Spin-orbit coupled spinor Bose–Einstein condensates, *Phys. Rev. Lett.* 105(16), 160403 (2010)

43. T. Kawakami, T. Mizushima, and K. Machida, Textures of $F = 2$ spinor Bose–Einstein condensates with spin-orbit coupling, *Phys. Rev. A* 84(1), 011607 (2011)
44. B. Ramachandhran, B. Opanchuk, X. J. Liu, H. Pu, P. D. Drummond, and H. Hu, Half-quantum vortex state in a spin-orbit-coupled Bose–Einstein condensate, *Phys. Rev. A* 85(2), 023606 (2012)
45. G. J. Conduit, Line of Dirac monopoles embedded in a Bose–Einstein condensate, *Phys. Rev. A* 86, 021605(R) (2012)
46. T. Kawakami, T. Mizushima, M. Nitta, and K. Machida, Stable skyrmions in $SU(2)$ gauged Bose–Einstein condensates, *Phys. Rev. Lett.* 109(1), 015301 (2012)
47. V. Achilleos, D. J. Frantzeskakis, P. G. Kevrekidis, and D. E. Pelinovsky, Matter-wave bright solitons in spin-orbit coupled Bose–Einstein condensates, *Phys. Rev. Lett.* 110(26), 264101 (2013)
48. Y. V. Kartashov, V. V. Konotop, and F. Kh. Abdullaev, Gap solitons in a spin-orbit-coupled Bose–Einstein condensate, *Phys. Rev. Lett.* 111(6), 060402 (2013)
49. Y. Xu, Y. Zhang, and B. Wu, Bright solitons in spin-orbit-coupled Bose–Einstein condensates, *Phys. Rev. A* 87(1), 013614 (2013)
50. H. Sakaguchi and B. Li, Vortex lattice solutions to the Gross–Pitaevskii equation with spin-orbit coupling in optical lattices, *Phys. Rev. A* 87(1), 015602 (2013)
51. D. A. Zezyulin, R. Driben, V. V. Konotop, and B. A. Malomed, Nonlinear modes in binary bosonic condensates with pseudo-spin-orbital coupling, *Phys. Rev. A* 88(1), 013607 (2013)
52. L. Salasnich and B. A. Malomed, Localized modes in dense repulsive and attractive Bose–Einstein condensates with spin-orbit and Rabi couplings, *Phys. Rev. A* 87(6), 063625 (2013)
53. Y. Cheng, G. Tang, and S. K. Adhikari, Localization of a spin-orbit-coupled Bose–Einstein condensate in a bichromatic optical lattice, *Phys. Rev. A* 89(6), 063602 (2014)
54. L. Salasnich, W. B. Cardoso, and B. A. Malomed, Localized modes in quasi-two-dimensional Bose–Einstein condensates with spin-orbit and Rabi couplings, *Phys. Rev. A* 90(3), 033629 (2014)
55. V. E. Lobanov, Y. V. Kartashov, and V. V. Konotop, Fundamental, multipole, and half-vortex gap solitons in spin-orbit coupled Bose–Einstein condensates, *Phys. Rev. Lett.* 112(18), 180403 (2014)
56. H. Sakaguchi and B. A. Malomed, Discrete and continuum composite solitons in Bose–Einstein condensates with the Rashba spin-orbit coupling in one and two dimensions, *Phys. Rev. E* 90(6), 062922 (2014)
57. S. Gautam and S. K. Adhikari, Vector solitons in a spin-orbit-coupled spin-2 Bose–Einstein condensate, *Phys. Rev. A* 91(6), 063617 (2015)
58. Y. Zhang, Y. Xu, and T. Busch, Gap solitons in spin-orbit-coupled Bose–Einstein condensates in optical lattices, *Phys. Rev. A* 91(4), 043629 (2015)
59. X. Zhu, H. Li, and Z. Shi, Defect matter-wave gap solitons in spin-orbit-coupled Bose–Einstein condensates in Zeeman lattices, *Phys. Lett. A* 380(40), 3253 (2016)
60. H. Lia, X. Zhua, and Z. Shi, Inverted solitons in a spin-orbit-coupled Bose–Einstein condensate, *Opt. Commun.* 392, 214 (2017)
61. L. Wen, Q. Sun, Y. Chen, D.-S. Wang, J. Hu, H. Chen, W.-M. Liu, G. Juzeliūnas, B. A. Malomed, and A.-C. Ji, Motion of solitons in one-dimensional spin-orbit-coupled Bose–Einstein condensates, *Phys. Rev. A* 94, 061602(R) (2016)
62. Y. Li and J. Xue, Stationary and moving solitons in spin-orbit-coupled spin-1 Bose–Einstein condensates, *Front. Phys.* 13(2), 130307 (2018)
63. G. Gligori, A. Maluckov, Lj. Hadzievski, S. Flach, and B. A. Malomed, Nonlinear localized flatband modes with spin-orbit coupling, *Phys. Rev. B* 94(14), 144302 (2016)
64. Y. V. Kartashov and V. V. Konotop, Solitons in Bose–Einstein condensates with helicoidal spin-orbit coupling, *Phys. Rev. Lett.* 118(19), 190401 (2017)
65. Y. Li, Y. Liu, Z. Fan, W. Pang, S. Fu, and B. A. Malomed, Two-dimensional dipolar gap solitons in free space with spin-orbit coupling, *Phys. Rev. A* 95(6), 063613 (2017)
66. H. Sakaguchi and B. A. Malomed, One- and two-dimensional gap solitons in spin-orbit-coupled systems with Zeeman splitting, *Phys. Rev. A* 97(1), 013607 (2018)
67. J. Dias, M. Figueira, and V. V. Konotop, Coupled nonlinear Schrödinger equations with a gauge potential: Existence and blowup, *Stud. Appl. Math.* 136(3), 241 (2016)
68. Sh. Mardonov, E. Ya. Sherman, J. Muga, H. W. Wang, Y. Ban, and X. Chen, Collapse of spin-orbit-coupled Bose–Einstein condensates, *Phys. Rev. A* 91(4), 043604 (2015)
69. H. Sakaguchi, B. Li, and B. A. Malomed, Creation of two-dimensional composite solitons in spin-orbit-coupled selfattractive Bose–Einstein condensates in free space, *Phys. Rev. E* 89(3), 032920 (2014)
70. H. Sakaguchi, E. Ya. Sherman, and B. A. Malomed, Vortex solitons in two-dimensional spin-orbit coupled Bose–Einstein condensates: Effects of the Rashba–Dresselhaus coupling and the Zeeman splitting, *Phys. Rev. E* 94(3), 032202 (2016)
71. G. Chen, Y. Liu, and H. Wang, Mixed-mode solitons in quadrupolar BECs with spin-orbit coupling, *Commun. Nonlinear Sci. Numer. Simul.* 48, 318 (2017)
72. Y. V. Kartashov, B. A. Malomed, V. V. Konotop, V. E. Lobanov, and L. Torner, Stabilization of spatiotemporal solitons in Kerr media by dispersive coupling, *Opt. Lett.* 40(6), 1045 (2015)

73. C. E. Bardyn, T. Karzig, G. Refael, and T. C. H. Liew, Topological polaritons and excitons in garden-variety systems, *Phys. Rev. B* 91(16), 161413 (2015)
74. A. V. Nalitov, D. D. Solnyshkov, and G. Malpuech, Polariton Z topological insulator, *Phys. Rev. Lett.* 114(11), 116401 (2015)
75. Y. V. Kartashov and D. V. Skryabin, Two-dimensional lattice solitons in polariton condensates with spin-orbit coupling, *Opt. Lett.* 41(21), 5043 (2016)
76. H. Sakaguchi, B. A. Malomed, and D. V. Skryabin, Spin-orbit coupling and nonlinear modes of the polariton condensate in a harmonic trap, *New J. Phys.* 19(8), 085003 (2017)
77. Y. C. Zhang, Z. W. Zhou, B. A. Malomed, and H. Pu, Stable solitons in three dimensional free space without the ground state: Self-trapped Bose–Einstein condensates with spin-orbit coupling, *Phys. Rev. Lett.* 115(25), 253902 (2015)
78. Y. Xu, Y. Zhang, and C. Zhang, Bright solitons in a two-dimensional spin-orbit-coupled dipolar Bose–Einstein condensate, *Phys. Rev. A* 92(1), 013633 (2015)
79. X. Jiang, Z. Fan, Z. Chen, W. Pang, Y. Li, and B. A. Malomed, Two-dimensional solitons in dipolar Bose–Einstein condensates with spin-orbit coupling, *Phys. Rev. A* 93(2), 023633 (2016)
80. B. Liao, S. Li, C. Huang, Z. Luo, W. Pang, H. Tan, B. A. Malomed, and Y. Li, Anisotropic semivortices in dipolar spinor condensates controlled by Zeeman splitting, *Phys. Rev. A* 96(4), 043613 (2017)
81. Y. A. Bychkov and E. I. Rashba, Oscillatory effects and the magnetic susceptibility of carriers in inversion layers, *J. Phys. C: Solid State Phys.* 17(33), 6039 (1984)
82. E. I. Rashba and E. Y. Sherman, Spin orbital band splitting in symmetric quantum wells, *Phys. Lett. A* 129(3), 175 (1988)
83. H. Sakaguchi and B. A. Malomed, Solitons in combined linear and nonlinear lattice potentials, *Phys. Rev. A* 81(1), 013624 (2010)
84. D. Kaup and B. Malomed, Soliton trapping and daughter waves in the Manakov model, *Phys. Rev. A* 48(1), 599 (1993)
85. Y. Li, Z. Luo, Y. Liu, Z. Chen, C. Huang, S. Fu, H. Tan, and B. A. Malomed, Two-dimensional solitons and quantum droplets supported by competing self- and cross-interactions in spin-orbit-coupled condensates, *New J. Phys.* 19(11), 113043 (2017)
86. C. Huang, Y. Ye, S. Liu, H. He, W. Pang, B. A. Malomed, and Y. Li, Excited states of two-dimensional solitons supported by spin-orbit coupling and field-induced dipole-dipole repulsion, *Phys. Rev. A* 97(1), 013636 (2018)
87. A. C. White, Y. Zhang, and T. Busch, Odd-petal-number states and persistent flows in spin-orbit-coupled Bose–Einstein condensates, *Phys. Rev. A* 95, 041604(R) (2017)
88. X. Zhang, M. Kato, W. Han, S. Zhang, and H. Saito, Spin-orbit-coupled Bose–Einstein condensates held under a toroidal trap, *Phys. Rev. A* 95, 033620 (2017)